https://doi.org/10.1016/j.ast.2018.07.026 This is the Pre-Published Version.

Intelligent GNSS/INS Integrated Navigation System for a Commercial UAV Flight Control System

Guohao Zhang and Li-Ta Hsu*

Interdisciplinary Division of Aeronautical and Aviation Engineering, The Hong Kong Polytechnic University, Kowloon, Hong Kong

Abstract

Owing to the increase in civil applications using quadcopters, commercial flight control systems such as Pixhawk are a popular solution to provide the sensing and control functions of an unmanned aerial vehicle (UAV). A low-cost global navigation satellite system (GNSS) receiver is crucial for the low-cost flight control system. However, the accuracy of GNSS positioning is severely degraded by the notorious multipath effect in mega-urbanized cities. The multipath effect cannot be eliminated but can be mitigated; hence, the GNSS/inertial navigation system (INS) integrated navigation is a popular approach to reduce this error. This study proposes an adaptive Kalman filter for adjusting the noise covariance of GNSS measurements under different positioning accuracies. The adaptive tuning is based on a proposed accuracy classification model trained by a supervised machine-learning method. First, principle component analysis is employed to identify the significant GNSS accuracy related features. Subsequently, the positioning accuracy model is trained based on a random forest learning algorithm with the labeled real GNSS dataset encompassing most scenarios concerning modern urban areas. To reduce the cases of misclassifying the GNSS accuracy, a fuzzy logic algorithm is employed to consider the GNSS accuracy propagation. Additionally, the process noise covariance of the INS is determined using the Allan variance analysis. The positioning performance of the proposed adaptive Kalman filter is compared with both a conventional Kalman filter and the positioning solution provided by the commercial flight control system, Pixhawk 2. The results show that the proposed adaptive Kalman filter using random forest with fuzzy logic can achieve a better classification of GNSS accuracy compared to the others. The overall positioning result improved by approximately 50% compared with the onboard solution.

Keywords: UAV; GPS; GNSS; Navigation; Kalman Filter; Adaptive Tuning; Machine Learning; Random Forest; Fuzzy Logic.

1. Introduction

Unmanned aerial vehicle (UAV) is increasingly used in civilian applications, such as disaster search and rescue [1], package delivery [2], and mapping of three-dimensional (3D) city models [3]. Localization is essential in UAV guidance, navigation, and control (GNC). Almost all outdoor UAVs are equipped with a global navigation satellite system (GNSS) receiver to provide their absolute location. A GNSS receiver receives and processes all the satellite signals to obtain the distances between the receiver and satellites, known as a pseudo-range. Subsequently, the pseudo-ranges are operated in conjunction with the satellite positions to determine the UAV position. The performance of the GNSS positioning is affected by several

* Corresponding author. Tel.: +852-3400-8061; fax: +852-2725-4922.
E-mail address: lt.hsu@polyu.edu.hk

factors, including satellite clock/orbit bias, atmospheric delay, and receiver thermal noise [4]. Currently, the biases caused by atmosphere and satellite orbit and clocks can be significantly corrected using a satellite-based augmentation system (SBAS) correction to achieve 1–2 m of positioning error in open-sky areas [5]. Inevitably, the low-attitude operating environment for an UAV becomes closer to civilians. In other words, it operates in the vicinity of urban cities or even inside urban areas. Compared to an open field, the urban configuration is denser and more complex. The urban configuration has caused many researchers to focus on using active sensors, including monocular/stereo cameras and light detection and ranging (LiDAR). Similar to the research development of autonomous driving vehicles, the LiDAR- and vision-sensor-based perception and localization became a major research stream in the UAV development. In 2012, a comprehensive survey focused on the GNC of an unmanned rotorcraft system was released [6]. It indicated that the actives sensors demonstrated their capabilities in obstacle detection [7], 3D mapping [8], and landing area detection [9]. In terms of localization, the LiDAR-based simultaneous localization and mapping could achieve submeter accuracy in a GNSS-denied area such as indoor environments [10]. With the 3D point cloud map in absolute coordinates, the LiDAR can also provide absolute localization. However, owing to the excessive computational load and memory expense, it is very difficult for the LiDAR-based rotorcrafts to perform well in applications that require a large area and long lifetime. In addition, the construction or preparation of the absolute 3D point cloud in a wide area requires expensive equipment and heavy manual calibration. Finally, the active sensor itself is too costly to be implemented in mass-market applications, including window-to-window parcel-delivery service. Vision odometry is also a popular option to provide a motion model to assist the dead reckoning (DR) of the UAV [11]. Vision odometry is similar to MEMS INS but with a slower accumulated error, i.e., it cannot estimate the absolute position [12]. Aerial mapping vehicles typically apply highly accurate GNSS/INS integrated receivers to provide submeter navigation service [13]. However, these high-end equipment require a geodetic grade dual-frequency GNSS antenna with a choke-ring design to mitigate multipath effects, high sampling rate dual-frequency GNSS receiver to eliminate ionosphere delay and tactical, and fiber optics INS to provide stable DR. Collectively, the price of the high-end equipment is within the range of 30,000 to 100,000 US dollars. In addition to the high cost, the weight of such equipment is approximately 2 kg to 4 kg. Therefore, it is clearly not suitable for consumer UAV in terms of the price budget and payload. Considering the factors listed above, the ideal sensor to provide absolute positioning is the consumer-grade GNSS receiver with single-frequency patch antenna that merely costs approximately 10 US dollars and 10 g of weight. For example, the popular Pixhawk flight control system (FCS) for quadcopters are embedded with a low-cost GNSS receiver and MEMS inertial measurement units (IMUs). The goal of this research is to improve the GNSS positioning performance for the low-cost FCS even in the highly urbanized HK central business district areas.

Hence, the cause of GNSS localization error must be addressed. GNSS satellites broadcast signals containing information of the satellite clock/orbit, and the transmit time. The signal passes through the atmosphere and is received by the receiver on Earth. Finally, the receiver's position can be estimated using the triangulation theory. In general, the triangulation is linearized by considering the first-order Taylor series and subsequently applying least squares to estimate the receiver position [14]. Several errors arise in the process, including ionospheric delay, tropospheric delay, satellite orbit/clock error, receiver thermal noise, and multipath effects. Differential GNSS (DGNSS) and real time kinematics (RTK) are technologies based on the principle that most error sources are differentiable between the GNSS reference station and aircrafts [15]. Thus, submeter or even centimeter levels of GNSS positioning can be achieved [16]. Unfortunately, in urban canyons, the GNSS signal suffers from signal blockages, diffraction, and reflection by buildings and skyscrapers, resulting in several tens of localization errors. These effects cannot be eliminated by differential technologies because the base station does not share the same signal reflection as the aerial rover. Currently, a universal model or a solution to solve this multipath effect and non-line-of-sight (NLOS) reception does not exist. Therefore, this phenomenon is the current impediment of the application of GNSS localization in an urbanized area [17]. The multipath and NLOS are currently the dominant errors of GNSS positioning in mega cities such as Hong Kong, Tokyo, and New York [18]. They can be severe and cause 70 m of GNSS

positioning error, as shown in Fig. 1(a). Compared with the distances between buildings in an urban area, this level of positioning performance is hazardous for UAVs, as shown in Fig. 1(b). The UAVs risk crushing on buildings owing to the erroneous GNSS positioning solutions. Hence, the multipath and NLOS error must be handled to achieve a safe and reliable UAV operation in urban areas [19]. The multipath effect can be mitigated by sophisticated GNSS antenna arrays [20-22], receiver correlator designs [23-25], and 3D city models [26-28]. However, a complete solution to eliminate this error does not exist. An effective solution is to integrate the onboard GNSS receiver with the inertial navigation system (INS) owing to their complementary [29].

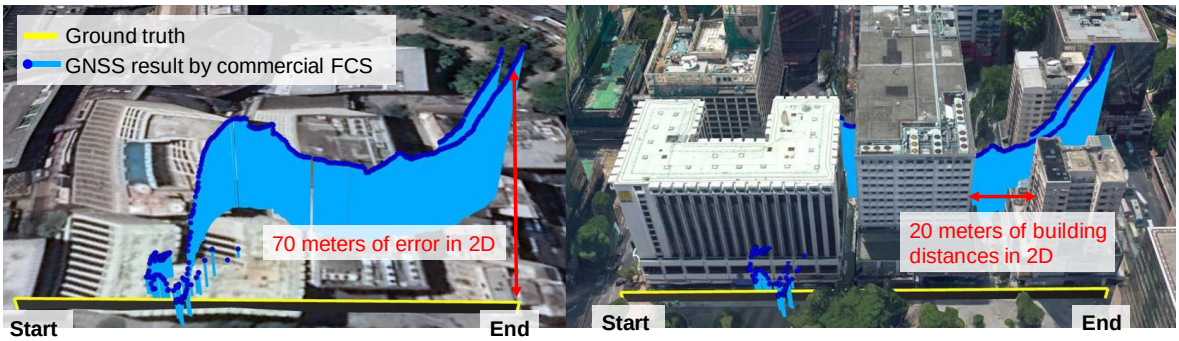

(a) (b)

Fig. 1. Demonstration of GNSS positioning error in urban areas (a) without and (b) with the appearances of 3D building model. The yellow and blue lines indicate the true trajectory and position solution of a GNSS receiver embedded in a commercial FCS, respectively.

The Kalman filter is widely employed to integrate the GNSS and INS with a balance between the two systems. Typically, the INS is used as a prediction, and the GNSS as a measurement. The tuning of both processes and measurement noise covariances will affect the Kalman gain, implying the weighting between system prediction and measurement update [30]. In general, the process noise covariance (***Q***) and measurement noise covariance (***R***) are fixed values, resulting in a constant weighting between the INS and GNSS. However, the operating environment (implying GNSS accuracy) is different in urban areas. Subsequently, constant tuning cannot yield an optimal performance. An adaptive tuning algorithm is required to describe the noise of the measurement model of the GNSS. A loosely coupled GPS/INS integration that tuned its ***R*** of the Kalman filter by the innovation/residual between the measurement and propagation is proposed [31]. To improve the residual-based adaptive Kalman filter (AKF), a quasi-accurate detection method is proposed to solve the noise generated by abrupt motion changes [32]. Hajiyev and Soken developed a robust AKF to isolate sensor/actuator faults by assigning multiple adaptive factors for both ***Q*** and ***R*** [33]. A cubature Kalman-filter-based multipath mitigation tracking system is developed for land-based navigation systems to remove the reflection components for distance measuring equipment (DME) measurement [34]. An initial alignment for the Strapdown INS/GNSS integrated system using AKF is recently proposed [35]. Gao et al. proposed a maximum posterior and random weighting approach to conquer the deficiency of the unscented Kalman filter for the INS/GNSS integrated navigation [36]. Recently, a fuzzy logarithmic least-squares method is proposed to handle the traditional analytic hierarchy of GPS accuracy for the AKF [37]. This method accurately evaluates the performance of their fusion algorithm, which is essential in multisensor integration. In this study, we propose an AKF-based INS/GNSS integration scheme specifically for commercial FCSs. In fact, a GNSS receiver provides several parameters, such as position dilution of precision (PDOP), numbers of satellite tracked, etc. The GNSS parameters are related to the operation environment of the GNSS receiver [38]. We developed an intelligent AKF that adjusts its ***R*** based on the FCS-output GNSS

parameters. The proposed AKF algorithm can achieve a better positioning accuracy than the conventional Kalman filter and the onboard positioning solution provided by Pixhawk 2.

The paper is organized as follows. Section II states the objective of this research. In section III, the details of the proposed AKF based on supervised machine learning is introduced. The experimental results are provided in section IV. Finally, the conclusions are presented in section V.

2. Problem Statement

2.1. Low-Cost Quadrotor UAV System

The quadrotor UAV has exhibited great potential in the past few years. One reason is its low cost in both mechanical and electrical components. Thus, we selected a self-assembled 99 mm × 99 mm quadrotor as the target UAV platform, as shown in Fig. 2(a). The flight control system is provided by one of the most popular low-cost autopilot avionics, Pixhawk 2, as shown in Fig. 2(b) [39]. Pixhawk 2 is embedded with a low-cost ublox NEO-M8N GNSS modular and MEMS IMU (LSM303D integrated accelerometers/magnetometers and L3GD20 gyroscopes) as shown in Fig. 2(c) and (d), respectively. During a flight, the avionics will store the flight information including the IMU raw measurements and GNSS measurements, barometer measurements, and magnetometer measurements.

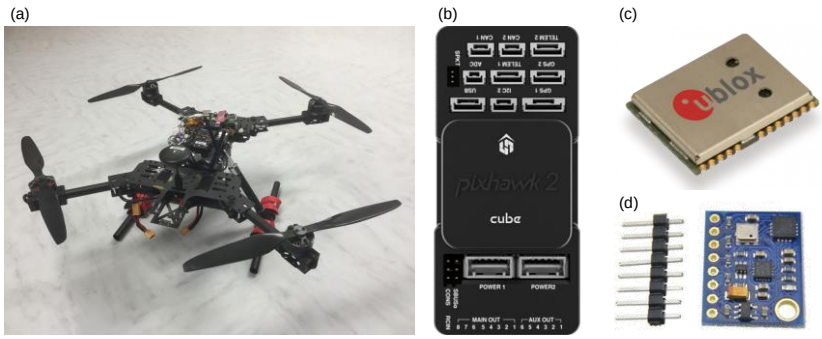

Fig. 2. (a) Self-assembled quadcopter; (b) Pixhawk 2 flight control system (with an autopilot software); (c) u-blox NEO-M8N GNSS chip; (d) MEMS IMU including LSM303D integrated accelerometers/magnetometers and L3GD20 gyroscopes.

In Pixhawk 2, the output GNSS measurement contains not only the 3D positioning solution but also the parameters relating to the GNSS positioning. The GNSS parameters and their corresponding meanings from the Pixhawk GNSS log data are shown in Table 1. The proposed adaptive tuning algorithm is developed based on the Pixhawk 2 as it is a well-known autopilot system. However, some of the features may have no relationship for classification and may even influence the classification accuracy. Therefore, the PCA technique is employed to select the major related features and aid in classification.

Table 1. GNSS measurements and parameters outputted by Pixhawk 2 flight control system

GPS Parameters outputted Pixhawk 2	Description	Unit
GPSTime	Time data with GPS week/second format	μs
Fix	GPS fixed mode	-
EPH	Standard deviation of horizontal positioning error	m
EPV	Standard deviation of vertical positioning error	m
Lat	Latitude solution	°
Lon	Longitude solution	°
Alt	Altitude solution	m

VelN	Velocity along N-axis in NED frame	m/s
VelE	Velocity along E-axis in NED frame	m/s
VelD	Velocity along D-axis in NED frame	m/s
nSat	Number of satellites for positioning	-
N	GPS noise	-
J	GPS jamming	-

2.2. Performance of the GNSS Solutions of Pixhawk 2 in Target UAV Operation Environments

We selected a dense urban area in Hong Kong that comprises many skyscrapers to evaluate the performance of the proposed AKF. According to the regulation of the Hong Kong civil aviation department, the UAV is banned for real flights in urban areas in Hong Kong. Thus, the data collection during the aerial vehicle operation was manually lifted and moved following the designed trajectory. Three experiment routes were conducted in the open sky, urban canyon 1, and urban canyon 2 scenarios, as shown in top of Fig. 3. As shown in the figure, the GNSS positioning performances are highly related to the operation environments. The open-sky environment is clean without surrounding buildings, i.e., almost no multipath effects. Consequently, the commercial GNSS receiver obtained satisfactory performance in open-sky areas while the other two did not. Notably, its positioning performance is very difficult to represent by a single GNSS parameter listed in Table 1. The objective of this paper is to classify the positioning error by a supervised machine learning method, and to adaptively adjust the measurement noise covariance of the AKF accordingly.

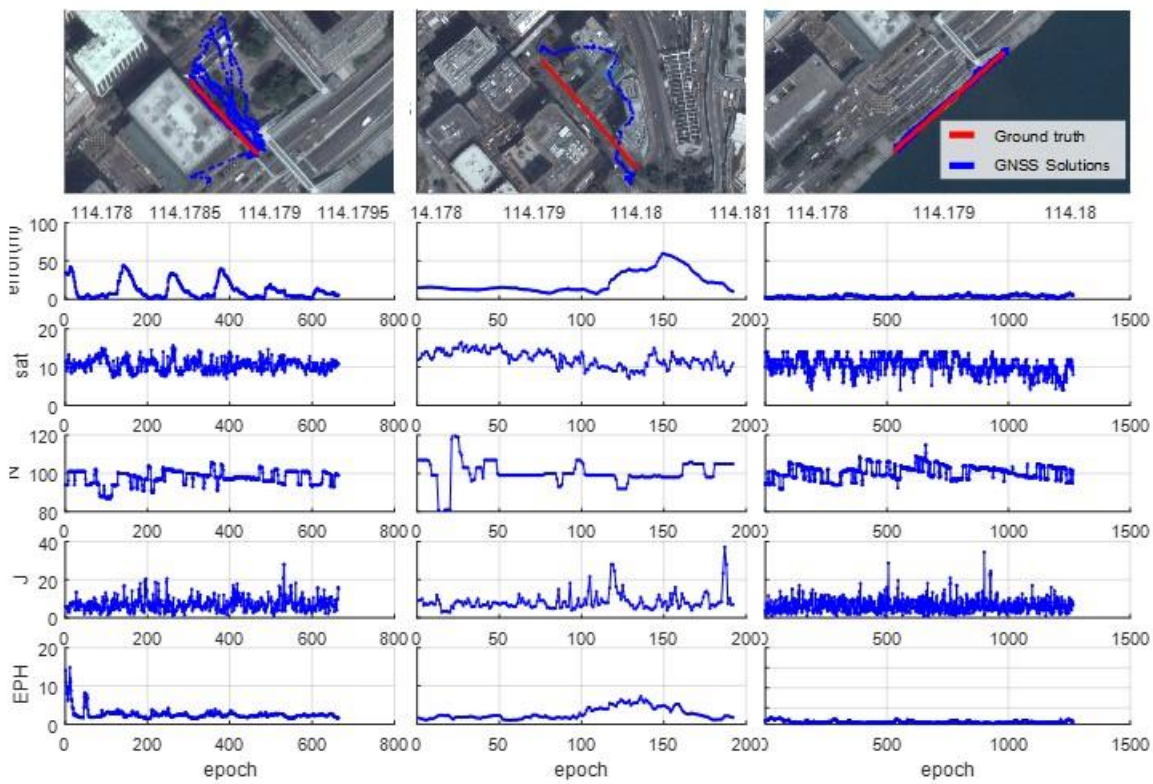

Fig. 3. Target UAV operation environments including (a) urban canyon scenario 1; (b) urban canyon scenario 2; (c) open-sky scenario. Red and blue lines in the top of the figure denote ground truth and positioning solutions provided by commercial GNSS receiver. The notations of error, sat, N, J, and EPH can be found in Table 1.

3. GNSS/INS Integration based Adaptive Kalman Filter

The flowchart of the proposed AKF is shown in Fig. 4. To adjust the measurement noise covariance $\boldsymbol{R}$ under different circumstances, it is important to classify the accuracy of the GNSS solutions provided by the commercial GNSS receiver. As shown in Fig. 3, the GNSS receiver provides several parameters related to the operation environment of the GNSS receiver. We first use principle component analysis (PCA) to disclose the significant features to reveal the accuracy of the GNSS solution. The relationship between the identified GNSS features and the labeled GNSS positioning accuracy can be derived by supervised machine-learning algorithms. The rationale behind this approach is that the complexity of the urban environments affects different GNSS parameters in inexplicitly. Consequently, the relationship becomes difficult to derive by analysis. The benefit of the machine-learning approaches is that the well-trained model could achieve acceptable classification accuracy without understanding the detailed relationship. Among the machine-learning algorithms, the proposed adaptive Kalman filter employs the random forest (RF) for the classification of the GNSS positioning accuracy. However, the model trained by the RF algorithm could still exhibit misclassifications owing to the out-of-sample error. This misclassification will influence the overall integration performance. During the UAV operation, the GNSS accuracy should change gradually instead of rapidly because most of the commercial GNSS receivers are implemented with a strong filter design. Consequently, the rapidly changed classification results could indicate misclassifications. In this study, we further employed a fuzzy logic algorithm to smooth the rapid changing classification and mitigate the misclassification error. Based on the proposed classification model of the GNSS positioning accuracy, the adaptive tuning of the measurement noise covariance of the proposed Kalman filter can be conducted. The process noise covariance, which is used model the uncertainty of INS, is determined by a sophisticated algorithm, i.e., the Allan variance analysis [40]. Finally, the proposed AKF is processed with the GNSS measurements, IMU inputs, and their noise covariance to calculate the navigation solution of the UAV.

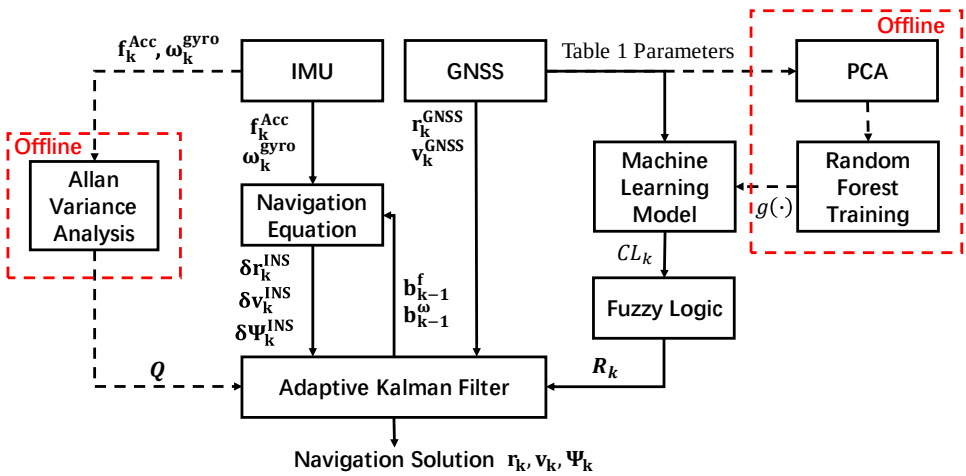

Fig. 4. Flowchart of the proposed Kalman filter with adaptive tuning. Solid and dash lines indicate online and offline operation, respectively.

3.1. System Formulation

To better demonstrate the performance of the proposed adaptive tuning of **R** and **Q**, a basic Kalman filter is selected in this study. The formulation is described as follows:

$$\hat{\mathbf{x}}_{\mathrm{k}}^{-} = \mathbf{F}_{\mathrm{k}}\hat{\mathbf{x}}_{\mathrm{k-1}}^{+} + \mathbf{u}_{\mathbf{k}} \tag{1}$$

$$\mathbf{P}_{\mathrm{k}}^{-} = \boldsymbol{\Phi}_{\mathrm{k-1}}\mathbf{P}_{\mathrm{k-1}}^{+}\boldsymbol{\Phi}_{\mathrm{k-1}}^{\mathrm{T}} + \mathbf{Q}_{\mathrm{k}} \tag{2}$$

$$\mathbf{K}_{\mathrm{k}} = \mathbf{P}_{\mathrm{k}}^{-}\mathbf{H}_{\mathrm{k}}^{\mathrm{T}}(\mathbf{H}_{\mathrm{k}}\mathbf{P}_{\mathrm{k}}^{-}\mathbf{H}_{\mathrm{k}}^{\mathrm{T}} + \mathbf{R}_{\mathrm{k}})^{-1} \tag{3}$$

$$\hat{\mathbf{x}}_{\mathbf{k}}^{+} = \hat{\mathbf{x}}_{\mathbf{k}}^{-} + \mathbf{K}_{\mathbf{k}}(\mathbf{z}_{\mathbf{k}} - \mathbf{H}_{\mathrm{k}}\hat{\mathbf{x}}_{\mathrm{k}}^{-}) \tag{4}$$

$$\mathbf{P}_{\mathbf{k}}^{+} = (\mathbf{I} - \mathbf{K}_{\mathrm{k}}\mathbf{H}_{\mathrm{k}})\mathbf{P}_{\mathrm{k}}^{-} \tag{5}$$

where the subscript denotes the k^{th} epoch, the superscript $^{+}$ denotes the state estimate after the measurement update, the subscript $^{-}$ denotes the state vector estimate after the state propagation but before the measurement update, and the caret $\hat{}$ indicates a Kalman filter estimate. **x** is the state vector consisting of the UAV's 3D position **r**, velocity **v**, attitude $\boldsymbol{\Psi}$, bias of 3D specific force $\mathbf{b}^{\mathbf{f}}$,and angular velocity $\mathbf{b}^{\boldsymbol{\omega}}$ as follows:

$$\mathbf{x} = \begin{bmatrix} \mathbf{r} \\ \mathbf{v} \\ \boldsymbol{\Psi} \\ \mathbf{b}^{\mathbf{f}} \\ \mathbf{b}^{\boldsymbol{\omega}} \end{bmatrix} \tag{6}$$

u is the system input provided by the INS, which is calculated by the navigation equations. The measurements of the MEMS IMU, angular rates, and specific forces, will be processed by the navigation equation to obtain the changes in attitude, velocity, and position of the UAV as follows [41]:

$$\mathbf{u} = \begin{bmatrix} \boldsymbol{\delta}\mathbf{r}^{\mathbf{INS}} \\ \boldsymbol{\delta}\mathbf{v}^{\mathbf{INS}} \\ \boldsymbol{\delta}\boldsymbol{\psi}^{\mathbf{INS}} \\ \mathbf{0} \\ \mathbf{0} \end{bmatrix} \tag{7}$$

z is the measurement provided by the commercial GNSS receiver as follows:

$$\mathbf{z} = \begin{bmatrix} \mathbf{r}^{\mathbf{GNSS}} \\ \mathbf{v}^{\mathbf{GNSS}} \\ \mathbf{0} \\ \mathbf{0} \\ \mathbf{0} \end{bmatrix} \tag{8}$$

H is the observation matrix and **F** is the system propagation model. Both **H** and **F** are used as a unity matrix in this integration. **P** is the state covariance. **K** is the Kalman gain. The details of the process **Q** and measurement noise covariance **R** are introduced in the following subsections.

3.2. GNSS Feature Identification - Principle Component Analysis (PCA)

PCA is a statistical method to observe the primary parameters from the dataset in the transformed dimension [38]. Using orthogonal transformations, a set of correlated parameters can be converted into a set of linear uncorrelated parameters, namely the principle components. Herein, it is employed to extract primary characteristic features of the GNSS parameter as indicated in Table 1. As the PCA can reduce the dimensions of multiple variables and convert the data into major dimensions, the GNSS parameters are processed with PCA to analyze their relationship with the positioning error. By selecting the first three principle components as the major three dimensions, the GNSS data after dimension transformation is as shown in Fig. 5. According to the PCA result, the colors of blue, cyan, green, and red are dominant. Thus, we separated the GNSS error into four classes as shown in Table 2. The PCA eigenvalue and eigenvector result is shown in Table 3. As shown, the major GNSS parameters related to the classification of the GNSS positioning error are EPH, EPV, nSat, N, and J. The extracted GNSS features, which are linear uncorrelated features PCA-1,2, and 3, will be used in the supervised machine-learning algorithms.

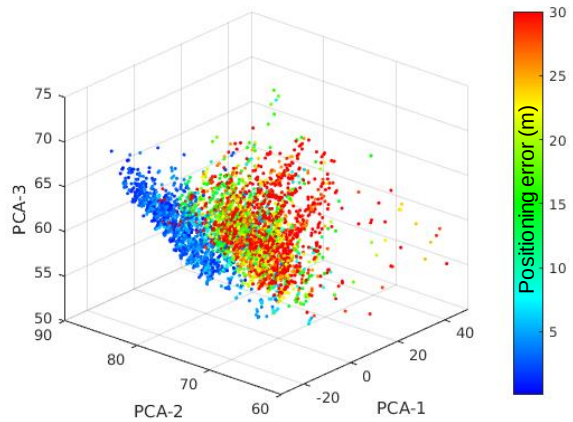

Fig. 5. Demonstration of the relationship between the GNSS positioning error and the extracted GNSS features by PCA. Colorbar indicates the corresponding positioning error.

Table 2. Definition of the classes of GNSS positioning accuracy.

Class	Positioning error
Healthy (HL)	below 5 m
Slightly shifted (SS)	5 to 13 m
Inaccurate (IA)	13 to 23 m
Dangerous (DG)	over 23 m

Table 3. Significance of GNSS parameters to first, second, and third principle component.

	PCA-1	PCA-2	PCA-3
EPH	0.023	0.214	0.242
EPV	0.067	0.488	0.718
VelN	0.001	0	0.029
VelE	0.003	0.011	0.021
VelD	0.004	0.012	0.053
nSat	0.038	0.331	0.208
N	0.184	0.754	0.613
J	0.976	0.193	0.051
Eigenvalue	399.0671	35.9236	9.9084

3.3. GNSS Positioning Error Classification – Random Forest Training

It is difficult to derive a linear function between the GNSS features and their positioning accuracy. A feasible method is to employ machine-learning techniques. Three types of machine-learning technique exist: supervised learning, unsupervised learning, and reinforcement learning. In supervised learning, the learner observes the training examples with inputs and the corresponding desired outputs, and subsequently obtains a general decision rule to predict the outputs from the new inputs. This paper employs the supervised machine-learning technique to predict the GNSS positioning error. In this study, the decision tree (DT) and random forest (RF) supervised machine-learning methods are applied.

The DT model represents a model that uses the input containing attribute values as a vector and returns an output value, namely the decision [42]. In a Boolean classification case, all outputs are defined as positive or negative. The node is an arbitrary feature. The branch is the value to split the input examples. The split example with mixed output will be further treated as a node with another feature for splitting, until all the branches have been separated into positive and negative. The major task is to explore an arrangement of feature nodes that split the examples well. The arrangement becomes a model used to predict with new inputs. To determine the arrangement order of the nodes, the Shannon entropy is employed to evaluate the information importance. The Shannon entropy is the expected value of the information contained in each of the message. It is used to calculate the information gain for determining the splitting-node order. In the classification of GNSS positioning error, the inputs are continuous values of different GNSS features; subsequently, the information gain of can be derived. The selection of the splitting node is to evaluate all the nodes with the corresponding information gain. By selecting the node with the highest information gain, the node will continue splitting with branches until all examples are separated as pure outputs. Finally, the node order is the training result of the DT.

The DT model could suffer from overfitting to the training set. A popular approach to handle this overfitting is the RF method [43]. RF is an ensemble learning method. It is constructed by multiple DTs with a subset of features to obtain a model for new data prediction. Its methodology can be described as following. Given training features $\mathrm{X}= \chi_1, \dots, \chi_n$ with the corresponding $\mathrm{Y} = y_1, \dots, y_n$, samples from X and Y will be separated into subsets of $\mathrm{X_d}$ and $\mathrm{Y_d}$ (well known as bootstrapping). Each subset is trained by a DT. The training result of the subset of features represents as a model of classification, namely $Y_d = g_d(X_d)$. The RF model is the ensemble of DTs, produced by averaging all individual DTs as shown below:

$$g^{RF}(\mathrm{X}) = \frac{1}{D}\sum_{d=1}^{D} g_d^{DT}(\mathrm{X_d}) = CL^{RF} \tag{9}$$

The bootstrapping process improves the model performance because the model variance is decreased while a similar bias is maintained. Each random tree is determined by a random set of data, which is highly uncorrelated. By averaging the tress, the variance can be mitigated in the training sets. To determine the size B of RF, cross validation is used to evaluate the model performance and the optimal number of trees is obtained. The cross validation is to exclude a small number of data subset during the model training and use that subset to verify the model accuracy. Herein, an RF model can be trained to classify the positioning error by labeling the GNSS features with their associated positioning errors. After obtaining the RF model that comprises multiple DTs, the new GNSS features are used to individually classify each tree in the forest. By averaging all the individual predictions of each tree, the mean value of the prediction indicates the final classified result from the given GNSS features.

3.4. Propagation of Classified GNSS Accuracy - Fuzzy Logic

Commercial GNSS chips typically comprise strong filters to obtain smoothed positioning solutions (because it is useful to most users). Consequently, the GNSS positioning error of the commercial GNSS chip

should change gradually instead of dramatically. However, the classified GNSS positioning error from the RF model could exhibit significant changes between two epochs because of the dramatic change in the GNSS features. In this study, a fuzzy logic approach is employed to handle the erroneous classification based on the nature of the smoothed error propagation. The fuzzy logic is implemented between two epochs (previous and current) of the classified results, and includes the fuzzification interface, decision making logic, and defuzzification interface. Fig. 6 shows its flowchart. The fuzzification interface converts a "crisp" value into a fuzzy "singleton." The probability is converted into a fuzzy number by a designated base rule and degree of membership (DOM) function, which are shown in Table 4 and Fig. 7, respectively. Herein, the DOM function is based on a linear interpolation. Both the input and output classes use the same DOM function because the fuzzy logic is used to propagate the class of GNSS accuracy.

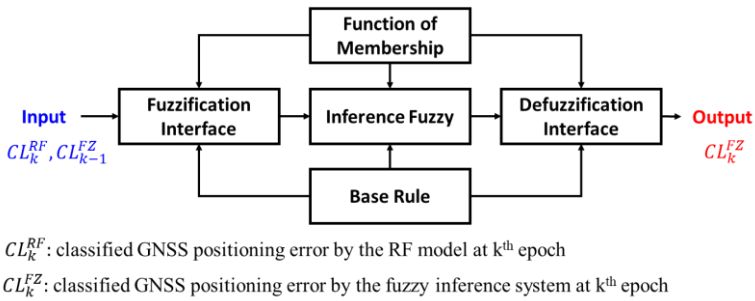

Fig. 6. Flowchart of the fuzzy logic algorithm. CL_k^{RF} is the classified GNSS positioning error by the RF model and CL_{k-1}^{FZ} and CL_k^{FZ} are the classified GNSS positioning errors of the precious and current epochs, respectively.

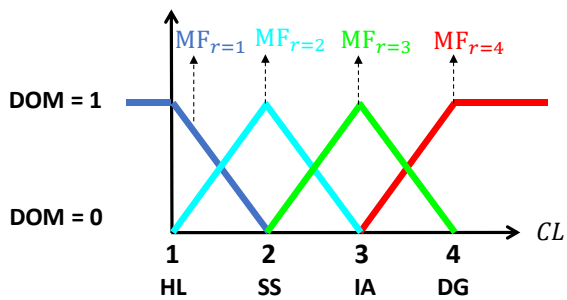

Fig. 7. Membership functions, μ_1, μ_2, μ_3, and $\mu_4$for both input and output classes of GNSS accuracy.

Table 4. Base rules of the fuzzy logic used in this paper. Healthy (HL), slightly shifted (SS), inaccurate (IA) and dangerous (DG) are used to indicate the accuracy of GNSS positioning solution. HL, SS, IA and DG are assigned as scalar value in 1, 2, 3, and 4, respectively.

c_2 \ c_1	HL (1)	SS (2)	IA (3)	DG (4)
HL (1)	HL (1)	HL (1)	SS (2)	SS (2)
SS (2)	HL (1)	SS (2)	SS (2)	IA (3)
IA (3)	SS (2)	IA (3)	IA (3)	DG (4)

(3) DG (4)	(2) IA (3)	(3) IA (3)	(3) DG (4)	(4) DG (4)

As shown in Table 4, there are 16 *rules* in the proposed fuzzy logic. The fuzzification is conducted by looking up the membership value of each rule. At each rule r at epoch k, the membership values of $\mu_{r,k}^{RF}$ and $\mu_{r,k-1}^{FZ}$ corresponding to CL_k^{RF} and CL_{k-1}^{FZ} can be estimated by (10) and (11), respectively.

$$\mu_{r,k}^{RF} = \mathrm{MF}_{r(c_1,c_2)}(CL_k^{RF}), c_{1,2} \in \{1,2,3,4\}, \tag{10}$$

$$\mu_{r,k-1}^{FZ} = \mathrm{MF}_{r(c_1,c_2)}(CL_{k-1}^{FZ}), c_{1,2} \in \{1,2,3,4\} \tag{11}$$

where MF denotes the membership function shown in Fig. 7. c_1 and c_2 denote the indexes of the class of membership function used for CL_k^{RF} and CL_{k-1}^{FZ}, respectively. An example is provided to explain the calculation of (10) and (11). If $c_1 = 1$ and $c_2 = 3$, the rule can be determined by $r(c_1, c_2)$ expressed in Table 4. Thus, $r(c_1 = 1, c_2 = 3) = 2$. Fig. 8 demonstrates the calculation of the membership value of $\mu_{r,k}^{RF} = \mathrm{MF}_{r=2}(CL_k^{RF} = 2.6)$. The red area indicated in the left of Fig. 8 is $\mu_{r,k}^{RF}$. Similarly, the membership value of $\mu_{r,k-1}^{FZ} = \mathrm{MF}_{r=2}(CL_{k-1}^{FZ} = 1.9)$ is the blue area indicated in the right of Fig. 8.

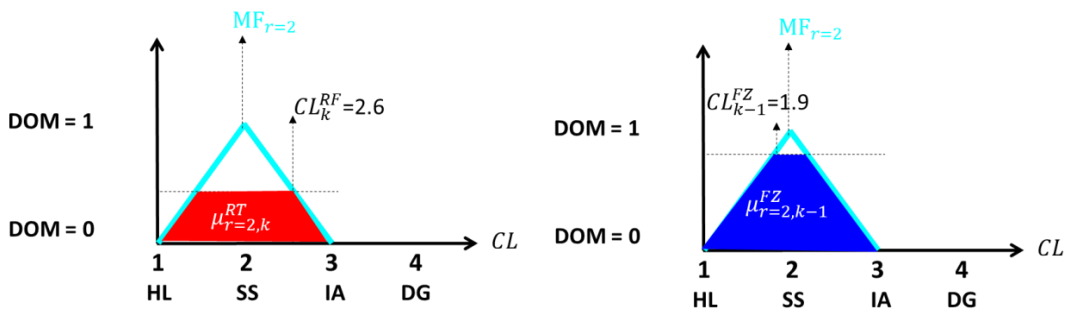

Fig. 8. Example of the calculation of membership values of $\mu_{r,k}^{RF}$ and $\mu_{r,k-1}^{FZ}$.

The weighting of each rule, r, is subsequently calculated by the aggregation of the two membership values of $\mu_{r,k}^{RF}$ and $\mu_{r,k-1}^{FZ}$, as shown in the equation below. Fig. 9 shows the calculation of the weighting based on the example provided in Fig. 8. As shown in Fig. 9, the weighting, $\alpha_{r,k}$, is the intersection of the two membership values.

$$\alpha_{r,k} = \mu_{r,k}^{RF} \wedge \mu_{r,k-1}^{FZ} \tag{12}$$

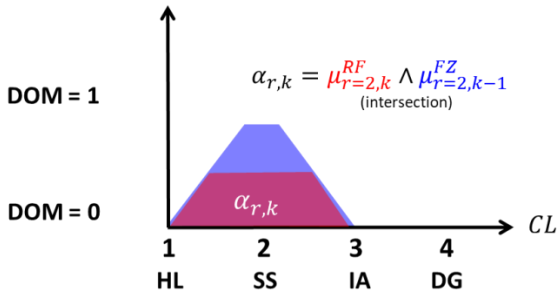

Fig. 9. Example of the calculation of weighting of each rule, $\alpha_{r,k}$.

Subsequently, the defuzzification process is used to estimate the weighted average of all the rules.

$$CL_k^{FZ} = \frac{1}{total\_rule} \sum_{r=1}^{total\_rule} \alpha_{r,k} \cdot CL_r \tag{13}$$

where $CL_r \in \{1,2,3,4\}$. Finally, the crisp output of the fuzzy logic is obtained. This output is a smoothed class of GNSS accuracy that will be used to adaptively estimate the **R** of the Kalman filter.

3.5. Adaptive Tuning of the Proposed Adaptive Kalman Filter

A crucial parameter of the Kalman filter is the ratio of the state error to the measurement noise covariance matrices (P/R). If the **P**/**R** is too small, the Kalman filter will converge slower than required. Conversely, if the **P**/**R** is overestimated, the Kalman filter would overestimate the measurement noise and might result in a rapid divergence from the truth. In general, the state noise matrix is initialized to the prediction of the error of state per epoch; subsequently, the measurement noise matrix is tuned until the Kalman filter is converged. By evaluating the collected GNSS data, an appropriate **R** value for different levels of GNSS accuracy (HL, SS, IA and DG) classified by RF and fuzzy logic can be obtained. The relationship between the fuzzy logic classified class CL_k^{FZ} and **R** is shown as Fig. 10. A class value exceeding 3.5 is considered a severe error case. An enormous **R** is set to minimize the contribution of the GNSS measurement in the integrated positioning system.

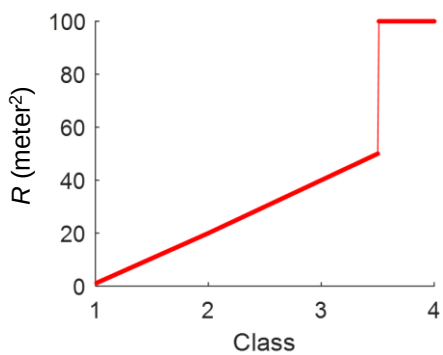

Fig. 10. Measurement noise covariance matrix **R** for the uncertainties of GNSS position with regards to the class derived by RF and fuzzy logic.

In general, the error characteristic of the IMU is not strongly correlated with its operating environments. The process noise covariance, which is used to describe the uncertainty of IMU sensors, is tuned in an offline process, as shown in Fig. 4. To construct the **Q**, the power spectral density (PSD) of the IMU should be computed. To avoid analyzing error characteristic in the complex frequency domain, the Allan variance analysis is adopted to substitute the frequency analysis by a time-domain estimation to observe the characteristic of the different errors of the IMU. The Allan variance is a time-domain analysis technique that is originally developed for the calibration of the frequency stability of oscillators [44]. It can be used to identify the characteristics of the underlying noise process, and can be applied to the error analysis of the IMU. The details of the Alan variance analysis for the IMU error can be found in [40]. We conducted a one-hour static experiment to process the Allan variance analysis. The result is shown in Fig 11. By analyzing the slope of the plot, the characteristic of the bias instability and random walk for both the accelerometers and gyroscopes can be estimated, and are indicated in Table 5. The values of the bias instability and random walk can be used to estimate the value of the process noise covariance matrix **Q** for the proposed AKF.

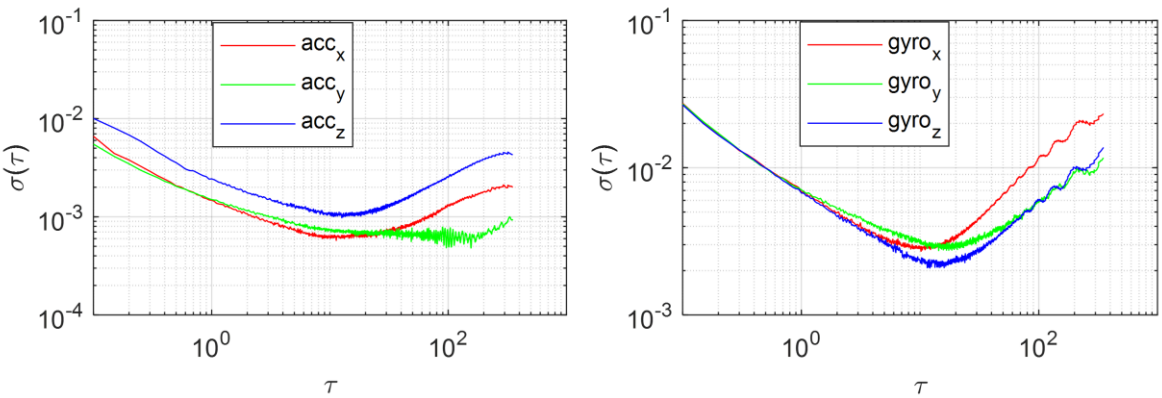

Fig. 11. Allan variance analysis of (a) three-axis accelerometers and (b) three-axis gyroscopes.

Table 5. Identified error coefficients for the MEMS-IMU embedded in Pixhawk 2 FCS.

Accelerometers			
	X	Y	Z
Bias Instability (m/s^2)	$5.7502e^{-4}$	$4.8152e^{-4}$	$9.7731e^{-4}$
Velocity Random Walk ($m/s^{3/2}$)	0.0014	0.0015	0.0024
Gyroscopes			
	X	Y	Z
Bias Instability ($^o/s$)	0.0027	0.0027	0.0021
Angular Random Walk ($^o/s^{1/2}$)	0.0068	0.0069	0.0067

4. Experimental Result

The proposed AKF is evaluated by post-processing the raw data logged by the Pixhawk 2. The raw collected data including the raw IMU data and the GNSS solutions will be processed as the inputs for the AKF. Five GNSS/INS integrated positioning results are compared:

1). commercial integrated positioning result obtained from Pixhawk FCS (PX4),
2). conventional (a fixed **R**) integrated positioning result (CKF),
3). integrated positioning result estimated by an AKF with decision tree model (DT),
4). integrated positioning result estimated by an AKF with random forest model (RF) and

5). The proposed integrated positioning result estimated by an AKF with RF and fuzzy logic model (RFFL).

As shown in Fig.12, three scenarios are tested and detailed in subsections, 4.1, 4.2, and 4.3, respectively.

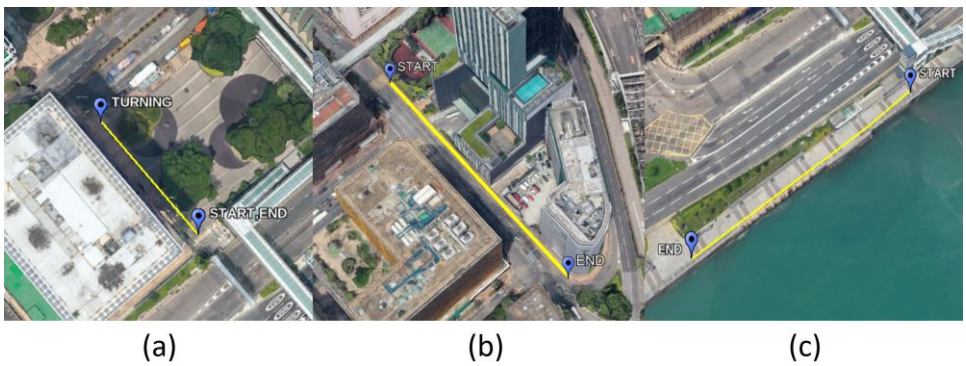

Fig. 12. Testing scenarios for the proposed integrated positioning system. (a) The urban scenario with turning route between two sides building; (b) The urban scenario with straight route between narrow buildings on two sides of the street; (c) The open-sky scenario with clear satellite visibility.

4.1. Experiment Result in Urban Canyon 1

The first experiment is to evaluate the positioning performance of the proposed AKF in an urban area; its environment is as shown in Fig. 12 (a). The trajectory begins from START and proceeds to the TURNING point; subsequently, the platform will experience a 180º turning and follow the same route to the END (same as START). The buildings are distributed along two sides of the trajectory. The positioning error of the GNSS chip on the FCS is shown in the top of Fig. 13. The labeled class of positioning error and the classified class by DT, RF, and the proposed RFFL are shown in the bottom of Fig. 13. The result shows the DT model only output the integer class for the GNSS positioning error, while the RF can predict the float class. The fuzzy logic can mitigate the large jump in the classes between two epochs, rendering the RFFL class similar to the labeled one. The corresponding R for the position state is shown in Fig. 14. The CKF uses a pretuned and fixed R value, while DT, RF, and RFFL are based on supervised machine learning to adaptively adjust the R value. As shown in Fig. 14, the machine-learning-trained models adjust the R with a small value while the GNSS error is small, and vice versa. The positioning results of the five GNSS/INS integrated positioning systems are shown in Fig. 15. The corresponding positioning errors are shown in Fig. 16. The mean and standard deviation (STD) of the positioning errors are summarized in Table 6. The positioning solution provided by Pixhawk experienced a large error (exceeding 40 m), and its error mean and STD are 10.2 m and 12.7 m, respectively. In other words, it is dangerous to use Pixhawk positioning to navigate the UAV operations in urban areas. The manually and carefully tuned **R** value of the CKF can significantly reduce the positioning error; however, it is still not satisfactory. The DT model adjusts the **R** value adaptively based on the condition of the GNSS measurement. It achieves a lower positioning error compared with the CKF. The RF model improves the classification accuracy of the DT model. The proposed RFFL AKF can achieve a better prediction of the class of GNSS error by implementing the fuzzy logic smoother. It also helps to mitigate the misclassification introduced positioning error during operation. The proposed RFFL AKF achieves a performance of 4.1 m and 3.9 m in the mean and STD of the positioning error, respectively. In addition, the maximum error of the proposed AKF is less than 15 m. Its solution outperforms the solution provided by the Pixhawk FCS.

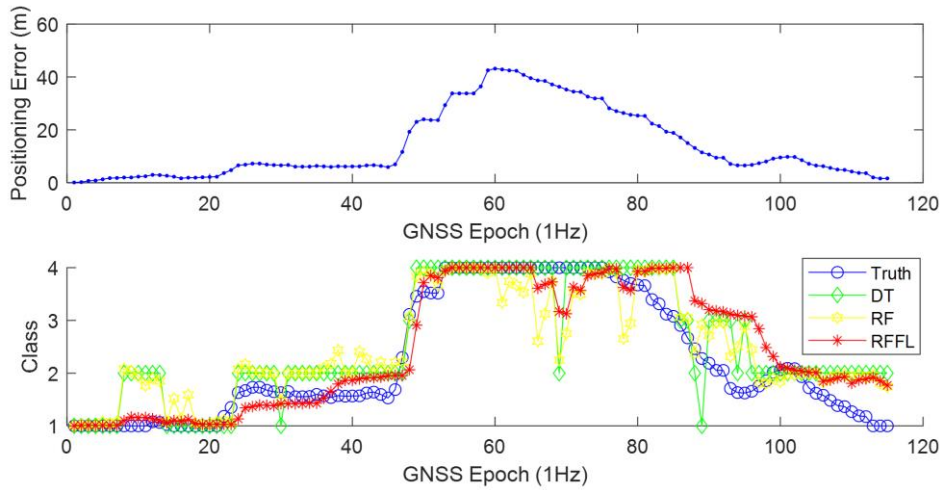

Fig. 13. Urban Test 1: Top panel indicates the positioning error of commercial GNSS chip on FCS. Bottom panel indicates the classification result of GNSS positioning error by different approaches.

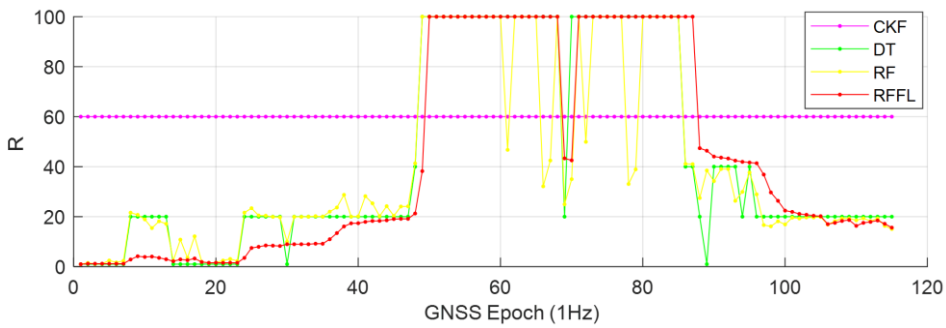

Fig. 14. Urban Test 1: Adaptive measurement noise covariance matrix **R** values of the position state based on different classification models.

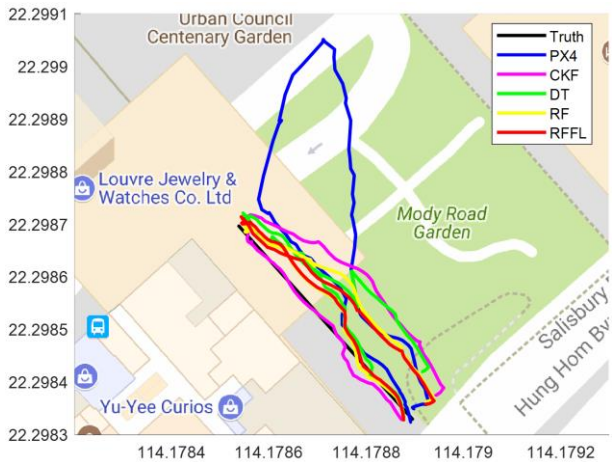

Fig. 15. Urban Test 1: Positioning result of the five GNSS/INS integrated positioning systems.

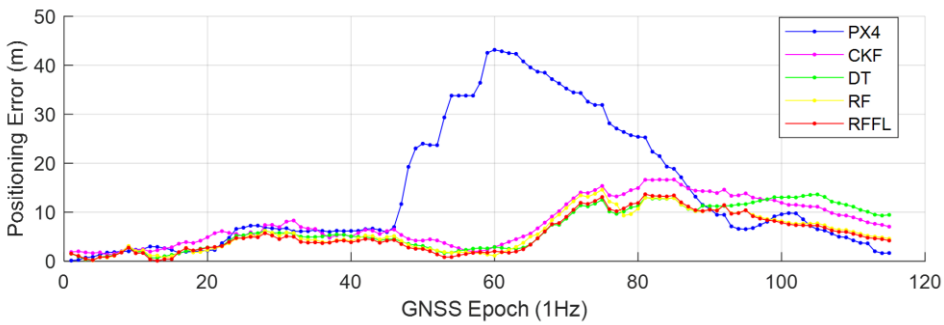

Fig. 16. Urban Test 1: Positioning error of the five GNSS/INS integrated positioning systems.

Table 6. Urban Test 1: Mean and STD of the positioning error of the five GNSS/INS integrated positioning systems.

	PX4	CKF	DT	RF	RFFL
Mean of Positioning Error (m)	10.2	5.7	4.9	4.3	4.1
STD of Positioning Error (m)	12.7	5.0	4.5	3.9	3.9

4.2. Experiment Result in Urban Canyon 2

The second experiment for evaluating the proposed AKF localization performance is conducted in the urban area, as shown in Fig. 12 (b). The trajectory begins from START and proceeds to the END point. The buildings are closely distributed along two sides of the trajectory. Compared to urban canyon 1, the distance between the buildings at two sides is shorter. Namely, it is a narrower urban canyon. The positioning error of the GNSS chip on the FCS is shown in the top of Fig. 17. The labeled class of the positioning error and the classified class by DT, RF, and the proposed RFFL are shown in the bottom of Fig. 17. As shown, DT, RF, and RFFL cannot achieve the similar results as demonstrated in section 4.1. During the 90th to 130th epoch, the classification results exhibit large classification error compared to the labeled class. The misclassification is caused by the similar GNSS parameters in the epochs of the large and small positioning errors. As shown in Fig. 18, the features of EPH, EPV, and J exhibit small values during the misclassification period. This causes

the machine-learning method continually classify them as good levels of GNSS positioning. Under this situation, the proposed AKF may adaptively use the inappropriate R, and further introduces positioning errors during this period. The corresponding measurement noise covariance matrix value **R** is shown in Fig. 19. Apart from the misclassification period, DT, RF, and RFFL adjust the **R** appropriately while the CKF maintains a fixed value. The positioning results of the five systems are compared in Fig. 20, and their positioning error is shown in Fig. 21. The mean and STD of the positioning errors are summarized in Table 7. The positioning solution provided by the FCS experienced a large error. Its mean and STD of error are 11.8 m and 12.2 m, respectively. The manually tuned **R** of the CKF yields better results compared to the Pixhawk result. It is worth noting that the **R** of the CKF is identical in both urban tests 1 and 2. However, as shown in Fig. 21, the CKF error continues accumulating. Consequently, the CKF result will be even worse as time progresses. The AKF can correctly adjust the **R** except at the abovementioned period. According to Table 7, the proposed method obtains the similar performance using the CKF. However, the CKF performance urban test 2 drifts while that of the proposed AKF does not.

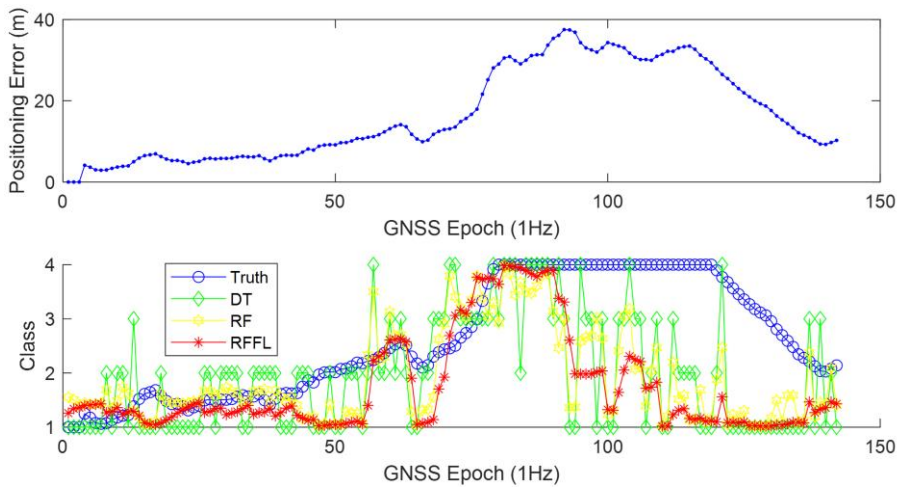

Fig. 17. Urban Test 2: Top panel indicates the positioning error of commercial GNSS chip on FCS. Bottom panel indicates the classification result of GNSS positioning error by different approaches.

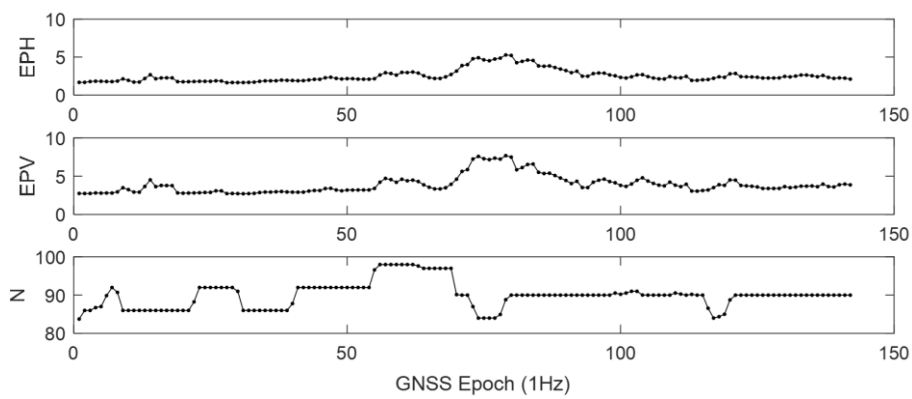

Fig. 18. Urban Test 2: Corresponding GNSS parameters including, EPH, EPV and N, for the machine learning based classifications.

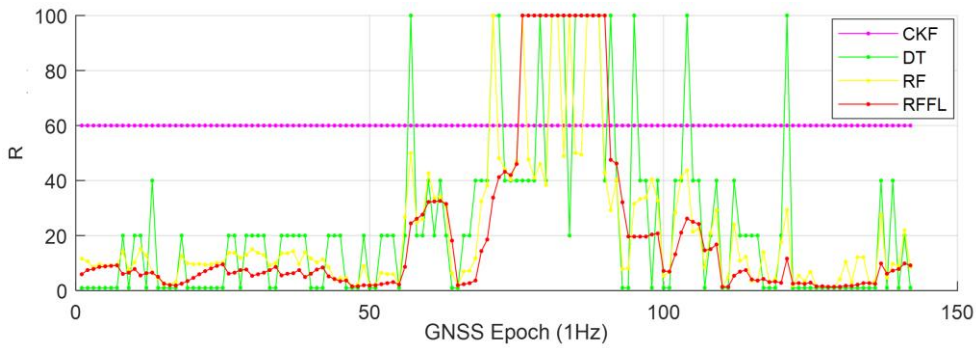

Fig. 19. Urban Test 2: Adaptive measurement noise covariance matrix R values of the position state based on different classification models.

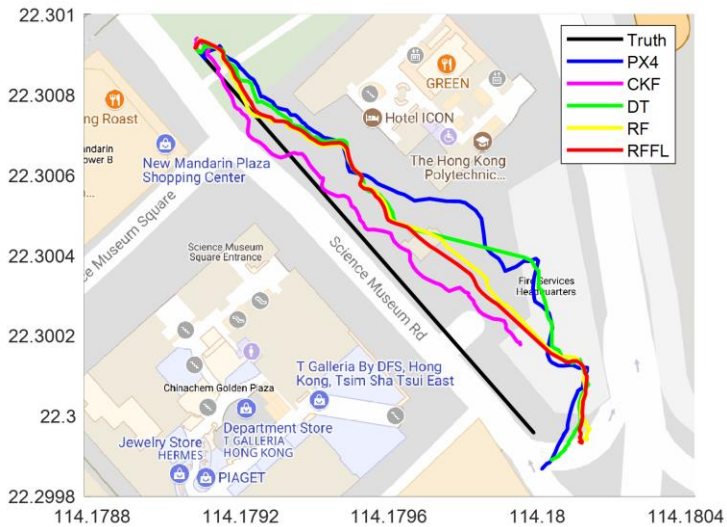

Fig. 20. Urban Test 2: Positioning result of the five GNSS/INS integrated positioning systems.

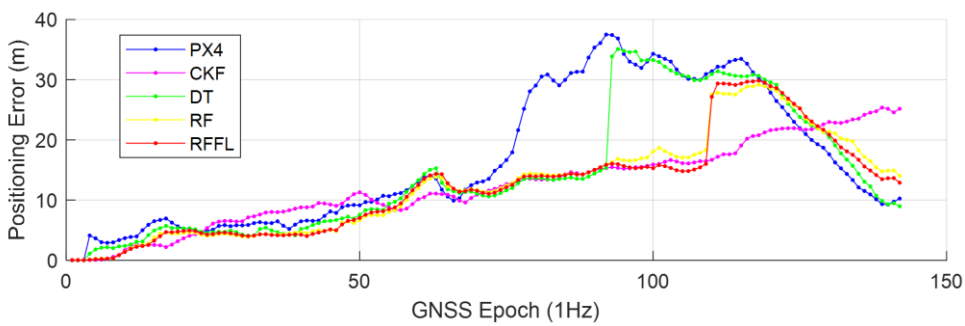

Fig. 21. Urban Test 2: Positioning error of the five GNSS/INS integrated positioning systems.

Table 7. Urban Test 2: Mean and STD of the positioning error of the five GNSS/INS integrated positioning systems.

	PX4	CKF	DT	RF	RFFL
Mean of Positioning Error (m)	11.8	8.8	10.1	8.8	8.6
STD of Positioning Error (m)	12.2	8.0	10.9	8.8	8.8

4.3. Open-sky Localization Result

An experiment is conducted to ensure the effectiveness of the proposed AKF in a regular environment, i.e., an open-sky area. The classification of the positioning error by RFFL is shown in Fig. 22, and its corresponding measurement noise covariance **R** is shown in Fig. 23. Because the platform is operated in an area with a high visibility of the GNSS satellite, the labeled class is the "healthy" class (the smaller value of the class, the healthier the measurement). The positioning error of the proposed AKF is shown in Fig. 24, and the trajectory is shown in Fig. 25. The mean and STD of the positioning errors are summarized in Table 8. The result of the proposed AKF is similar to the result from Pixhawk FCS, achieving accurate positioning solution for the open-sky area. The result verifies the proposed AKF can maintain the accurate positioning in general operations.

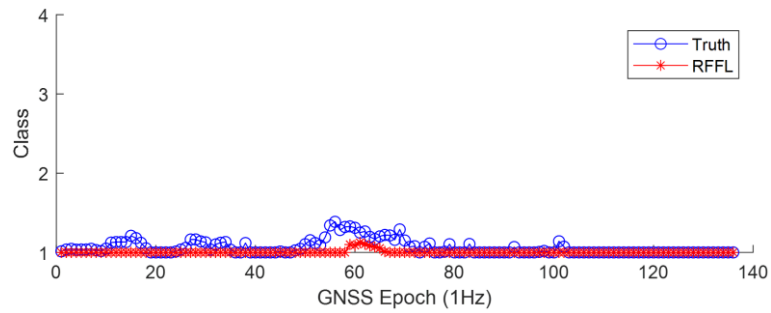

Fig. 22. Open-sky Test: Labeled class and classification result of RFFL.

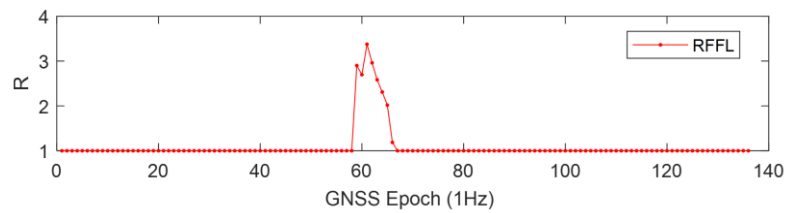

Fig. 23. Open-sky Test: Adaptive measurement noise covariance matrix R values of the position state based on RFFL.

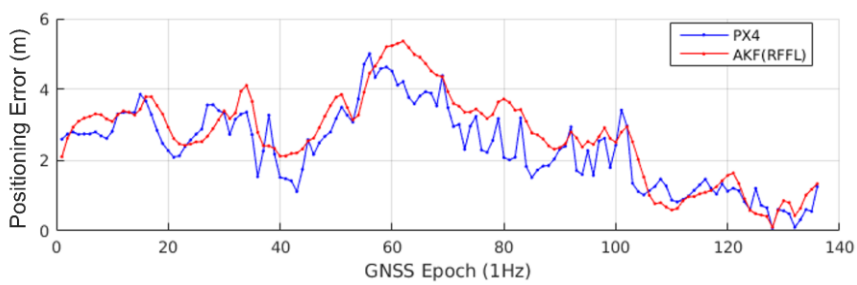

Fig. 24. Open-sky Test: Positioning error of the Pixhawk system and the proposed RFFL AKF.

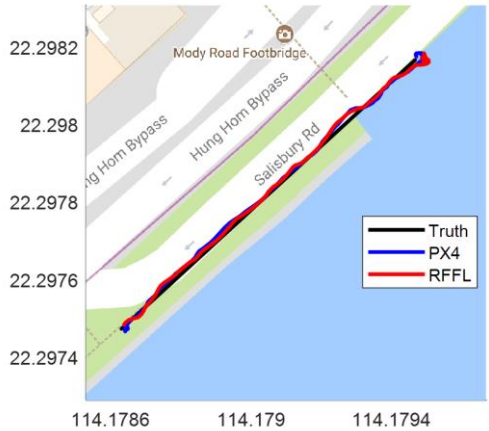

Fig. 25. Open-sky Test: Positioning result of the Pixhawk system and the proposed RFFL AKF.

Table 8. Open-sky Test: Mean and STD of the positioning error of Pixhawk system and the proposed RFFL AKF.

	PX4	RFFL
Mean of Positioning Error (m)	2.2	2.4
STD of Positioning Error (m)	1.1	1.2

5. Conclusions and Future Work

Commercial FCSs such as Pixhawk are crucial to apply UAVs to civil applications. GNSS positioning solutions provided by commercial GNSS chips embedded on FCSs are satisfactory for UAVs flying a few hundreds of feet from the ground. However, it is not sufficiently accurate to safely operate in an aircraft in urban areas with a high density of tall buildings. One straightforward solution is to integrate the GNSS solution with the INS. In this study, UAV positioning was first improved by integrating the GNSS/INS based on the conventional Kalman filter scheme. Subsequently, the adaptive Kalman filter was proposed to adaptively adjust the measurement noise covariance **R,** which implies the quality of the GNSS solution. To predict the quality, supervised machine-learning algorithms, including the decision tree and random forest, were employed. The classification model of the positioning error was trained with the data that included almost all the operation areas in the Hong Kong testbed. In addition, fuzzy logic was developed to smooth the predicted class from the trained models by considering the classification result of the previous and current epochs. Based on the smoothed classified result from the fuzzy logic, the measurement noise covariance can be adaptively tuned. According to the experimental results, the proposed integrated AKF GNSS/INS can effectively identify the level of GNSS error and improve the positioning result of the UAV.

It is worth noting that the proposed AKF was designed based on Pixhawk FCS; however, the proposed idea can also be implemented with other integrated GNSSs/INSs by replacing the GNSS parameters provided in Table 1.

In some cases, the proposed AKF could fail to correctly adjust the measurement noise covariance. This occurs when the GNSS parameters output by the GNSS chip of Pixhawk are the same for both the epochs, with accurate and inaccurate GNSS solutions. In other words, the features are not sufficient to distinguish (or represent) the accuracy of the GNSS solutions. For future work, we plan to explore the relationship between

the quality of the GNSS solution and the raw pseudo-range, as well as the carrier-to-noise ratio and dilution of precession.

Acknowledgements

The authors acknowledge the fund from the “Fundamental Research on Free Exploration Category of Shenzhen Municipal Science and Technology Innovation Committee” to support the project, “Localization Strategy using Low-Cost GNSS Module for UAV” (Project No. JCYJ20170818103653507) and this research.

References

[1] J. Sun, B. Li, Y. Jiang, C.-y. Wen, A Camera-Based Target Detection and Positioning UAV System for Search and Rescue (SAR) Purposes, Sensors, 16 (2016) 1778.
[2] G. Hoareau, J.J. Liebenberg, J.G. Musial, T.R. Whitman, Package transport by unmanned aerial vehicles, Google Patents, 2017.
[3] M. Javanmardi, E. Javanmardi, Y. Gu, S. Kamijo, Towards High-Definition 3D Urban Mapping: Road Feature-Based Registration of Mobile Mapping Systems and Aerial Imagery, Remote Sensing, 9 (2017) 975.
[4] P. Misra, P. Enge, Global Positioning System: Signals, Measurements, and Performance, Ganga-Jamuna Press, Lincoln, MA 01773 2011.
[5] P. Enge, T. Walter, S. Pullen, K. Changdon, C. Yi-Chung, T. Yeou-Jyh, Wide area augmentation of the Global Positioning System, Proceedings of the IEEE, 84 (1996) 1063-1088.
[6] F. Kendoul, Survey of advances in guidance, navigation, and control of unmanned rotorcraft systems, Journal of Field Robotics, 29 (2012) 315-378.
[7] R. Joshua, A. Jayesh, B. Jovan, K. Yeonsik, H. Karl, H. Jason, P. Scott, A Real-Time Obstacle Detection and Reactive Path Planning System for Autonomous Small-Scale Helicopters, AIAA Guidance, Navigation and Control Conference and Exhibit, American Institute of Aeronautics and Astronautics2007.
[8] S. Siebert, J. Teizer, Mobile 3D mapping for surveying earthwork projects using an Unmanned Aerial Vehicle (UAV) system, Automation in Construction, 41 (2014) 1-14.
[9] Z. Yu, K. Nonami, J. Shin, D. Celestino, 3D Vision Based Landing Control of a Small Scale Autonomous Helicopter, International Journal of Advanced Robotic Systems, 4 (2007) 51-56.
[10] S. Grzonka, G. Grisetti, W. Burgard, Towards a navigation system for autonomous indoor flying, Robotics and Automation, 2009. ICRA '09. IEEE International Conference on, 2009, pp. 2878-2883.
[11] J. Kelly, S. Saripalli, G.S. Sukhatme, Combined Visual and Inertial Navigation for an Unmanned Aerial Vehicle, in: C. Laugier, R. Siegwart (Eds.) Field and Service Robotics: Results of the 6th International Conference, Springer Berlin Heidelberg, Berlin, Heidelberg, 2008, pp. 255-264.
[12] J. Wendel, O. Meister, C. Schlaile, G.F. Trommer, An integrated GPS/MEMS-IMU navigation system for an autonomous helicopter, Aerospace Science and Technology, 10 (2006) 527-533.
[13] J. Wozencraft, D. Millar, Airborne Lidar and Integrated Technologies for Coastal Mapping and Nautical Charting, Marine Technology Society Journal, 39 (2005) 27-35.
[14] E. Kaplan, C. Hegarty, Understanding GPS: principles and applications, Artech house2005.
[15] B. Pervan, F.C. CHAN, D. GEBRE‐EGZIABHER, S. Pullen, P. Enge, G. Colby, Performance Analysis of Carrier‐Phase DGPS Navigation for Shipboard Landing of Aircraft, Navigation, 50 (2003) 181-191.
[16] R.B. Langley, Rtk gps, GPS World, 9 (1998) 70-76.
[17] M.G. Petovello, P.D. Groves, Multipath vs. NLOS signals, Inside GNSS, 8 (2013) 40-42.
[18] L.-T. Hsu, Analysis and modeling GPS NLOS effect in highly urbanized area, GPS Solutions, 22 (2017) 7.
[19] G. Zhang, L.-T. Hsu, A New Path Planning Algorithm Using a GNSS Localization Error Map for UAVs in an Urban Area, Journal of Intelligent & Robotic Systems, DOI 10.1007/s10846-018-0894-5(2018).
[20] P. Closas, C. Fernandez-Prades, A Statistical Multipath Detector for Antenna Array Based GNSS

Receivers, IEEE Transactions on Wireless Communications, 10 (2011) 916-929.
[21] Z. Jiang, P. Groves, NLOS GPS signal detection using a dual-polarisation antenna, GPS Solutions, 18 (2014) 15-26.
[22] N. Kubo, K. K, L.-T. Hsu, O. Amai, Multipath Mitigation Technique under Strong Multipath Environment Using Multiple Antennas, Journal of Aeronautics, Astronautics and Aviation, Series A, 49 (2017) 75-82.
[23] V.A. Veitsel, A.V. Zhdanov, M.I. Zhodzishsky, The Mitigation of Multipath Errors by Strobe Correlators in GPS/GLONASS Receivers, GPS Solutions, 2 (1998) 38-45.
[24] P.C. Fenton, J. Jones, The theory and performance of NovAtel Inc.'s vision correlator, Proceedings of the ION GNSS, 2005, pp. 2178-2186.
[25] L.-T. Hsu, Integration of Vector Tracking Loop and Multipath Mitigation Technique and its Assessment, ION GNSS+ 2013, Nashville, TN, 2013, pp. 3263-3278.
[26] P.D. Groves, Shadow Matching: A New GNSS Positioning Technique for Urban Canyons, The Journal of Navigation, 64 (2011) 417-430.
[27] L.-T. Hsu, Y. Gu, S. Kamijo, 3D building model-based pedestrian positioning method using GPS/GLONASS/QZSS and its reliability calculation, GPS Solutions, 20 (2016) 413–428.
[28] R. Yozevitch, B.b. Moshe, A Robust Shadow Matching Algorithm for GNSS Positioning, Navigation, 62 (2015) 95-109.
[29] J.Z. Sasiadek, Sensor fusion, Annual Reviews in Control, 26 (2002) 203-228.
[30] T. Tominaga, N. Kubo, Adaptive Estimation of Measurement Noise to Improve the Performance of GNSS Single Point Positioning in Dense Urban Environment, Journal of the Institute of Positioning, Navigation and Timing of Japan, 8 (2017) 1-8.
[31] A. Almagbile, J. Wang, W. Ding, Evaluating the performances of adaptive Kalman filter methods in GPS/INS integration, Journal of Global Positioning Systems, 9 (2010) 33-40.
[32] X. Luo, H. Wang, Robust Adaptive Kalman Filtering – a method based on quasi-accurate detection and plant noise variance–covariance matrix tuning, Journal of Navigation, 70 (2017) 137-148.
[33] C. Hajiyev, H.E. Soken, Robust Adaptive Kalman Filter for estimation of UAV dynamics in the presence of sensor/actuator faults, Aerospace Science and Technology, 28 (2013) 376-383.
[34] M. Liu, J. Lai, Z. Li, J. Liu, An adaptive cubature Kalman filter algorithm for inertial and land-based navigation system, Aerospace Science and Technology, 51 (2016) 52-60.
[35] D. Wang, H. Lv, J. Wu, In-flight initial alignment for small UAV MEMS-based navigation via adaptive unscented Kalman filtering approach, Aerospace Science and Technology, 61 (2017) 73-84.
[36] Z. Gao, D. Mu, S. Gao, Y. Zhong, C. Gu, Adaptive unscented Kalman filter based on maximum posterior and random weighting, Aerospace Science and Technology, 71 (2017) 12-24.
[37] X. Wang, X. Wang, J. Zhu, F. Li, Q. Li, H. Che, A hybrid fuzzy method for performance evaluation of fusion algorithms for integrated navigation system, Aerospace Science and Technology, 69 (2017) 226-235.
[38] N.M. Drawil, H.M. Amar, O.A. Basir, GPS Localization Accuracy Classification: A Context-Based Approach, IEEE Transactions on Intelligent Transportation Systems, 14 (2013) 262-273.
[39] E. Ebeid, M. Skriver, J. Jin, A Survey on Open-Source Flight Control Platforms of Unmanned Aerial Vehicle, Digital System Design (DSD), 2017 Euromicro Conference on, IEEE, 2017, pp. 396-402.
[40] N. El-Sheimy, H. Hou, X. Niu, Analysis and Modeling of Inertial Sensors Using Allan Variance, IEEE Transactions on Instrumentation and Measurement, 57 (2008) 140-149.
[41] P.D. Groves, Principles of GNSS, Inertial, and MultiSensor Integrated Navigation Systems (GNSS Technology and Applications), 2nd ed., Artech House Publishers2013.
[42] S.R. Safavian, D. Landgrebe, A survey of decision tree classifier methodology, IEEE Transactions on Systems, Man, and Cybernetics, 21 (1991) 660-674.
[43] A. Liaw, M. Wiener, Classification and regression by randomForest, R news, 2 (2002) 18-22.
[44] J.A. Barnes, A.R. Chi, L.S. Cutler, D.J. Healey, D.B. Leeson, T.E. McGunigal, J.A. Mullen, W.L. Smith, R.L. Sydnor, R.F.C. Vessot, G.M.R. Winkler, Characterization of Frequency Stability, IEEE Transactions on Instrumentation and Measurement, IM-20 (1971) 105-120.